



Microstructure and Properties of Al₂O₃-13wt.%TiO₂-Reinforced CoCrFeMnNi High-Entropy Alloy Composite Coatings Prepared by Plasma Spraying

Shuaishuai Zhu^{1,2} · Zhijia Zhang^{1,2} · Baosen Zhang^{1,2} · Yaqui Yu^{1,2} · Zhangzhong Wang^{1,2} · Xiancheng Zhang³ · Bin Lu⁴

Submitted: 28 July 2020 / in revised form: 31 December 2020 / Accepted: 19 January 2021 / Published online: 5 February 2021
© ASM International 2021

Abstract This study deals with Al₂O₃-13wt.%TiO₂-reinforced CoCrFeMnNi high-entropy alloy (HEA) composite coatings prepared by plasma spraying. The effect of the Al₂O₃-TiO₂ ceramic phase on the microstructure, mechanical properties and high-temperature tribological performance of the as-sprayed composite coatings was investigated. The results showed that the composite coatings consisted of a HEA phase with a FCC (face-centered cubic) structure and an Al₂O₃-TiO₂ ceramic phase with a three-dimensional network structure. The coatings presented a typical layered structure with less porosity than pure HEA coatings. The three-dimensional network structure was mainly due to partially melted Al₂O₃-13wt.%TiO₂ particles during the spraying process. The composite coating with Al₂O₃-TiO₂ ceramic phase had an improved plastic deformation resistance and a reduced elastic recovery resistance. Its wear rate was lower than that of the pure HEA coating. The main wear mechanisms included oxidation, wear and adhesive wear. The Al₂O₃-TiO₂ ceramic phase reduced the adhesive wear and

promoted the tribological behavior of the HEA composite coating at low temperature. The excellent wear resistance of the as-sprayed coating at high temperatures was mainly due to the formation of an oxide layer on the worn surface.

Keywords Al₂O₃-13wt.%TiO₂ · high-entropy alloy coating · high-temperature tribological performance · microstructure · plasma spray

Introduction

High-entropy alloys (HEAs) are advanced solid solution alloys that contain five or more principal elements in equimolar or nearly equimolar ratios. Recently, HEAs have developed into the most promising novel metal materials because of the advantages of structural stability, mechanical properties, corrosion resistance and wear resistance (Ref 1-3), which are directly related to the effects of high entropy, sluggish diffusion, severe lattice distortion and combined effects. However, it is difficult to control the homogeneity of bulk HEAs due to the properties of the multiple principal elements, and the bulk HEAs are mainly prepared by arc melting technology or casting methods. Thus, the size of the bulk HEAs is limited. Recently, large-area HEA coatings (HEACs) have attracted attention with the possibility of the critical applications in industrial engineering due to their good corrosion resistance and wear resistance (Ref 4-6).

Plasma spraying is a versatile and widely applied technique to prepare all kinds of coatings due to the higher spraying temperature and efficiency (Ref 7-9), and some researchers have fabricated HEA films and coatings by this technique. The flattening and rapid cooling process can promote the densification of coatings with lamellar structures and produce high adhesion strength (Ref 10). Ang et al. (Ref 11) successfully

Shuaishuai Zhu and Zhijia Zhang share the first authorship of this paper.

✉ Baosen Zhang
baosenzhang@njit.edu.cn

¹ School of Materials Science and Engineering, Nanjing Institute of Technology, Nanjing 211167, China

² Jiangsu Key Laboratory of Advanced Structural Materials and Application Technology, Nanjing 211167, China

³ School of Mechanical and Power Engineering, East China University of Science and Technology, Shanghai 200237, China

⁴ Haian Hengyi Sliding Bearing Co., Ltd, Nantong 226600, China

prepared the lamellar-structure CoCrFeMnNi HEACs by plasma spraying and found that the coatings showed an anisotropic mechanical response due to the unique lamellar microstructure. Wang et al. (Ref 12) reported that a plasma-sprayed CrMnFeCoNi HEA coating exhibited a single-phase face-centered cubic (FCC) solid solution with appropriate spraying parameters, and the overall porosity percentage of the coating was calculated as $\sim 2.9\%$. Xiao et al. (Ref 10) prepared single-phase FCC CoCrFeMnNi HEACs by plasma spraying with different spraying parameters, and found that the wear resistance of the CoCrFeMnNi HEACs was enhanced by the high cohesive strength among splats and the increase in oxides in the coating. However, some studies indicated that the hardness value of single-phase FCC CoCrFeMnNi HEACs was only 212 HV \sim 423 HV (Ref 13, 14), and the application of the CoCrFeMnNi HEA coatings is limited by their low hardness values.

Most studies show that high hardness improves wear resistance of HEA coatings (Ref 15, 16). The coating hardness can be significantly enhanced by the in situ synthesis and addition of ceramic phases or intermetallic compounds (Ref 17). Al₂O₃ with a hexagonal structure is easy to be produced at the friction interface, which is beneficial for increasing the plastic deformation resistance of an HEA coating during sliding at elevated temperatures (Ref 18). In addition, Al₂O₃ and TiO₂ promote the formation of a dense

oxide film at high temperatures (Ref 19, 20). Therefore, the TiO₂ and Al₂O₃ ceramic phases are the most promising reinforcement phases to enhance the wear resistance of the HEA coatings at elevated temperatures. Moreover, some studies on the high-temperature wear behaviors of HEAs present different wear mechanisms compared to those at room temperature (Ref 21, 22). The phase structure of the HEA coating was stable during high-temperature sliding, and the oxide films on the worn surface significantly improved the wear resistance (Ref 23, 24). Furthermore, the grain refinement of the subsurface layer caused by dynamic recrystallization under thermal–mechanical stress sliding at high temperature has a significant effect on the wear resistance (Ref 25). Herein, conventional Al₂O₃-13wt.%TiO₂ ceramic powders were introduced into CoCrFeMnNi coatings by plasma spraying, and the microstructure, mechanical properties and high-temperature wear behavior of the composite coating were analyzed.

Materials and Methods

Coatings Preparation

Figure 1(a) and (b) shows the scanning electron microscopy (SEM) morphology of CoCrFeMnNi HEA powders

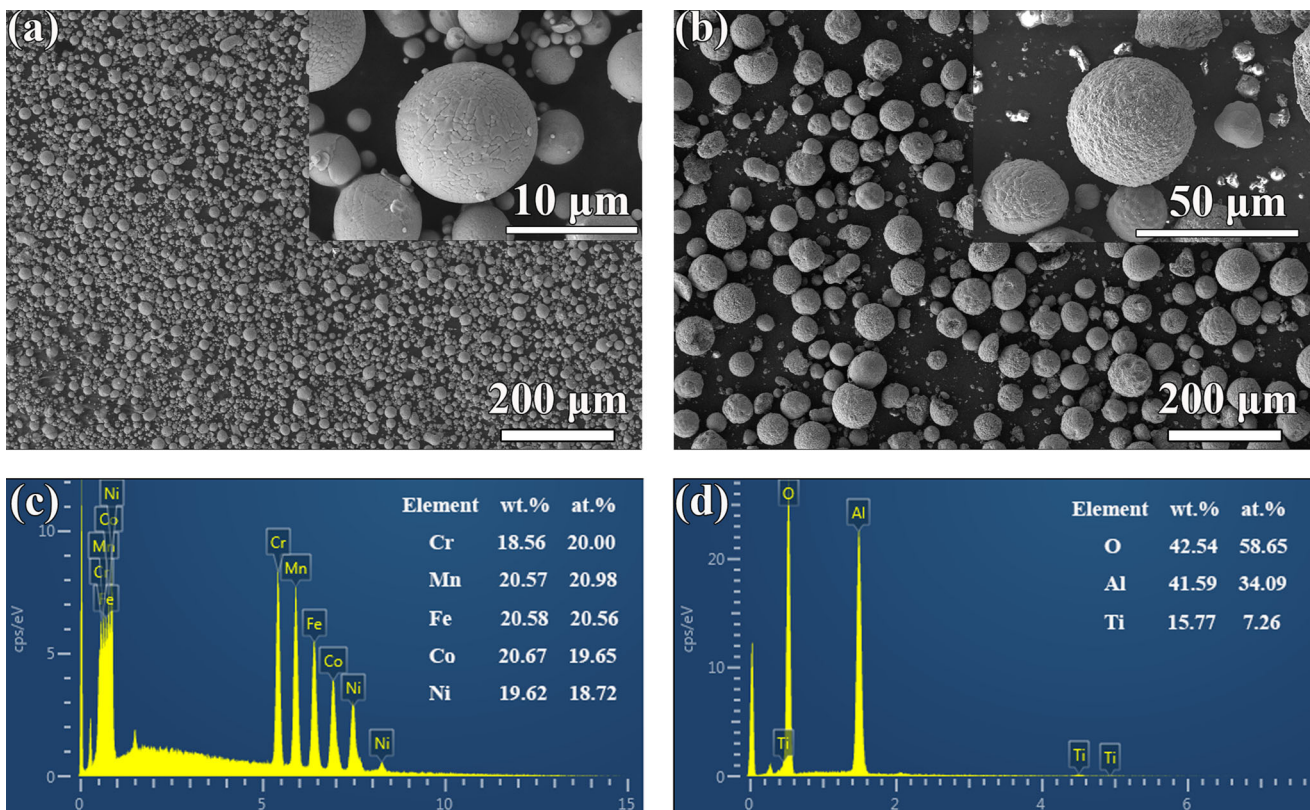


Fig. 1 (a) Al₂O₃-13wt.%TiO₂ powders, (b) CoCrFeMnNi HEA powders and (c, d) the chemical composition of the powders

Table 1 Detailed parameters of plasma spraying

Parameters	Values
Spraying system	Sulzer Metco 7 MB, USA
Spraying current, A	600
Spraying voltage, V	75
Primary gas (Ar) flow rate, L min ⁻¹	70
Secondary gas (H ₂) flow rate, L min ⁻¹	7
Carrier gas(Ar) flow rate, L min ⁻¹	12
Powder feed rate, g min ⁻¹	30
Spraying distance, mm	150
Scanning rate, mm s ⁻¹	1000
Spraying times (passes)	21

(~ 25 μm) and Al₂O₃-13wt.%TiO₂ powders (abbreviated to AT13 hereafter, ~ 15 μm). The size of powders is uniform, and the spherical particles facilitate the flow of powders. The chemical analysis of the CoCrFeMnNi HEA and AT13 powder via energy-dispersive spectrometer (EDS, shown in Fig. 1c and d) was almost identical to the elemental composition given by the supplier. In this research, the HEA powders were mixed with 10 wt.% AT13 powders for 4 h in a 3D motion mixer to prepare the feedstock powders, and the motion frequency of the mixer was 50 Hz. The pure CoCrFeMnNi coating (denoted as the HEA coating) and the CoCrFeMnNi/(Al₂O₃-TiO₂) composite coating (denoted as the HEA-10 coating) were deposited by plasma spraying. The substrate was commercial mild steel with a chemical composition of C: 0.2, Mn: 0.45, Si: 0.15, P: 0.03, S: 0.05, and Fe: balance, wt.%. Table 1 shows the detailed plasma spraying parameters.

Characterization Methods

A field emission transmission electron microscope (FETEM, FEI TECNAI G2 F20, USA) and field emission scanning electron microscope (FESEM, Zeiss Merlin Compact, Germany) equipped with an EDS were used to investigate the coating cross section morphology and structure. X-ray diffraction (XRD, Ultima IV, Rigaku) using Cu Kα radiation at 40 kV and 40 mA at a scan rate of 4°/min, ranging from 20° to 100°, was used to study the phase composition of the as-sprayed coatings. An Agilent G200 nanoindenter (USA) equipped with a Berkovich diamond tip (TB21090) was used to perform nanoindentation on the coatings at room temperature. The constant loading rate was 0.5 mN·s⁻¹, the maximum load was 50 mN, and the holding time was 10 s. The unloading rate was the same as loading rate. The hardness of the as-sprayed coatings was tested by a Vickers hardness tester (Future-Tech FM-700). The hardness measurements were

conducted with a load of 300 gf and a spacing of 50 μm between each measuring point, and the measuring points were mainly the HEA matrix.

Friction and Wear Performance

The wear behavior of the as-sprayed coatings was tested by a multifunctional tribometer (Rtec, MFT-3000, USA) with rotary ball-on-disk dry sliding from 25 to 600 °C, respectively. A Si₃N₄ ceramic ball (diameter of 9.5 mm) slid against the prepolished coating surfaces. The surface roughness (Ra) before the tribological tests of the wear specimens was 0.058 μm. The constant applied normal load was 50 N, the rotating speed was 300 rpm, the rotation radius was 3 mm, the linear velocity at wear marks was approximately 94 mm/s, and the sliding duration was 1200 s. The wear rate (W_r) was determined by the formula: $W_r = V/FS$, where V is the wear volume measured by a 3D profiler (Rtec, Micro-XAM, USA), F is the loading force, and S is the sliding distance. Tribological tests of each sample were repeated three times under the same conditions, and the average results were reported.

Results and Discussion

Microstructure and Mechanical Properties of Coatings

Figure 2 shows the XRD patterns of the powders and the as-sprayed HEA coatings. The AT13 powders displayed the α-Al₂O₃ phase (JCPDS No. 10-0173) and rutile TiO₂ phase (JCPDS No. 21-1276). The diffraction peaks of the as-sprayed coatings corresponded to the face-centered cubic (FCC) HEA solid solution (JCPDS No. 47-1417), which was the same as those reported in previous studies. This reveals that the as-sprayed HEA coating matrix both was composed of an FCC single-phase solid solution. Thus, the addition of AT13 powders had no effect on the HEA matrix structure. The α-Al₂O₃ phase (JCPDS No. 10-0173) and γ-Al₂O₃ phase (JCPDS No. 10-0425) were present in the HEA-10 coating. Therefore, some α-Al₂O₃ transformed to metastable γ-Al₂O₃ during plasma spraying due to the lower critical nucleation free energy of γ-Al₂O₃, than of α-Al₂O₃, which promoted the formation of the nano-Al₂O₃-TiO₂ phase (Ref 26). The diffraction peaks of TiO₂ were not prominent because of the low content of TiO₂ in the composite coatings. The diffraction peaks of the oxides, also shown in Fig. 2, corresponded to the in-flight oxidation of the HEA particles during spraying. The peaks of oxides corresponded to AB₂O₄ (A, B = Ni, Co, Fe, Cr or Mn)-type mixed oxides, and the results were supported by previous experiments. (Ref 10-12, 27)

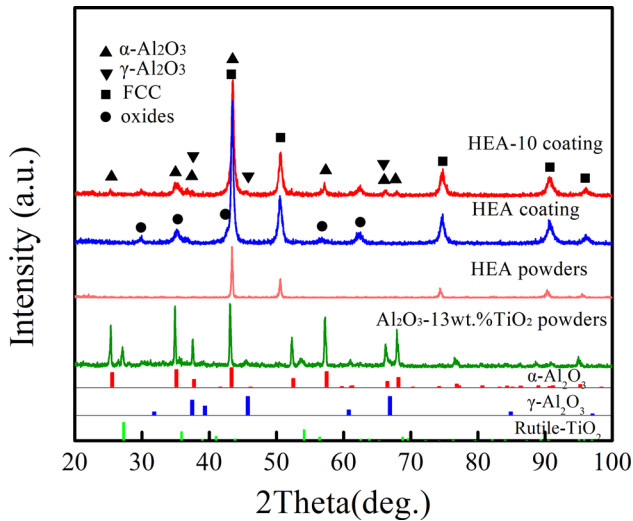


Fig. 2 XRD patterns of powders and coatings

Figure 3 shows the cross-sectional microstructures of the as-sprayed coatings. Figure 3(a) and (b) shows the overview images of the coatings. The overall porosity percentages of the pure HEA coating and the HEA-10 composite coating were calculated to be 3.79 and 1.25%,

respectively. Figure 3(c) and (d) shows the local magnification microstructures of the HEA coating and HEA-10 composite coating, respectively. The cross-sectional microstructures indicate that the pure HEA coating and the HEA-10 composite coating both presented flat and bent layered structures. Therefore, both HEA and Al_2O_3 -13wt.% TiO_2 particles can be well melted during the plasma spraying process. These high-speed flying molten particles splattered and fragmented during deposition to form the layered structure. Additionally, a few microcracks were present in the coatings. Table 2 shows the chemical compositions of different areas of the as-sprayed coatings. The EDS results indicate that a large amount of Mn and a small amount of Cr were lost during burning and oxidation in the spraying process. The EDS maps of the HEA-10 composite coating (Fig. 4) show that Fe, Co and Ni were uniformly distributed mainly in the coating matrix, while some Mn, Cr and O elements were enriched together. The above EDS analyses show that Mn and Cr elements were more susceptible than the other elements to oxidation during the plasma spraying process. Combined with the XRD results (Fig. 2), it was found that the oxides in the as-sprayed coating were MnCr_2O_4 and MnO. Furthermore, the EDS

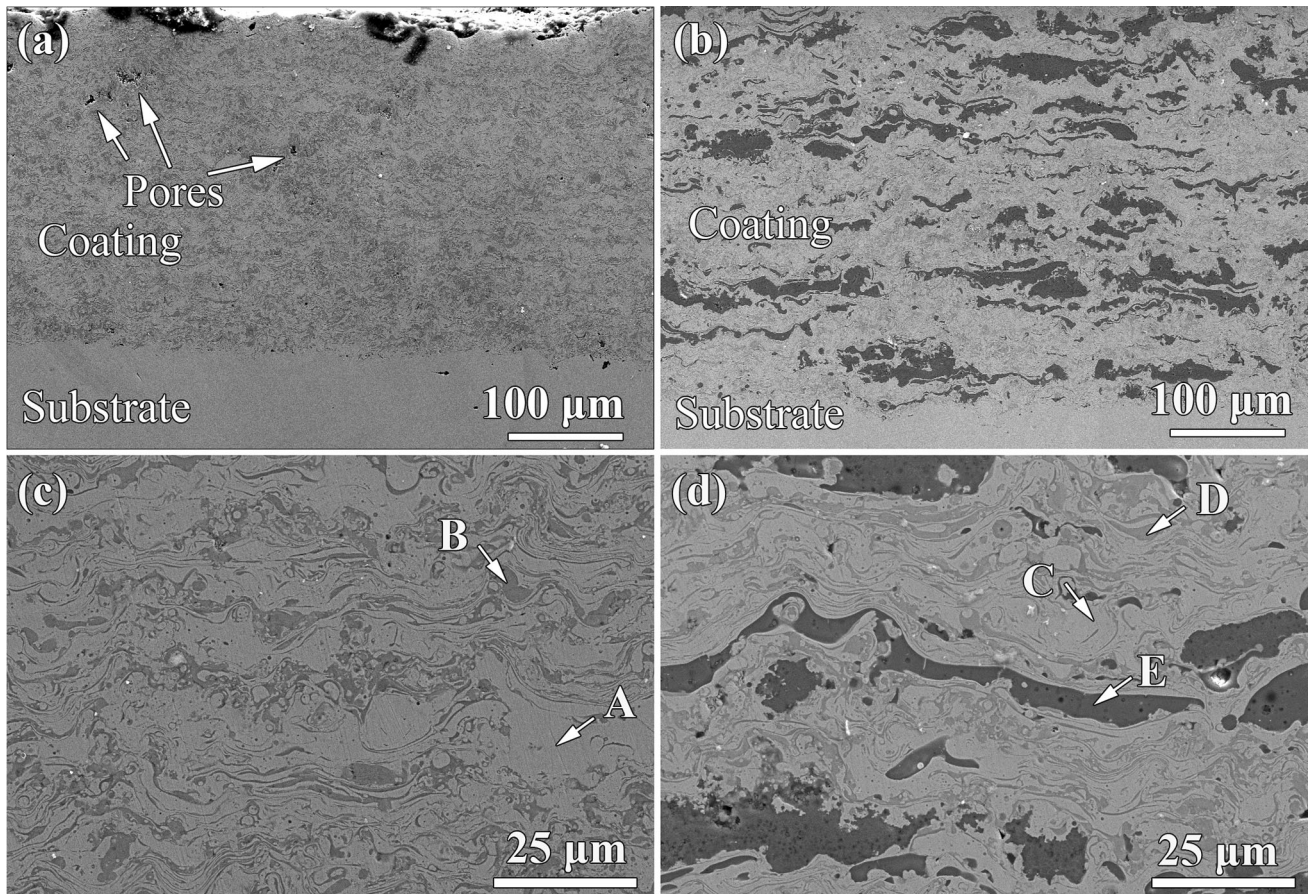
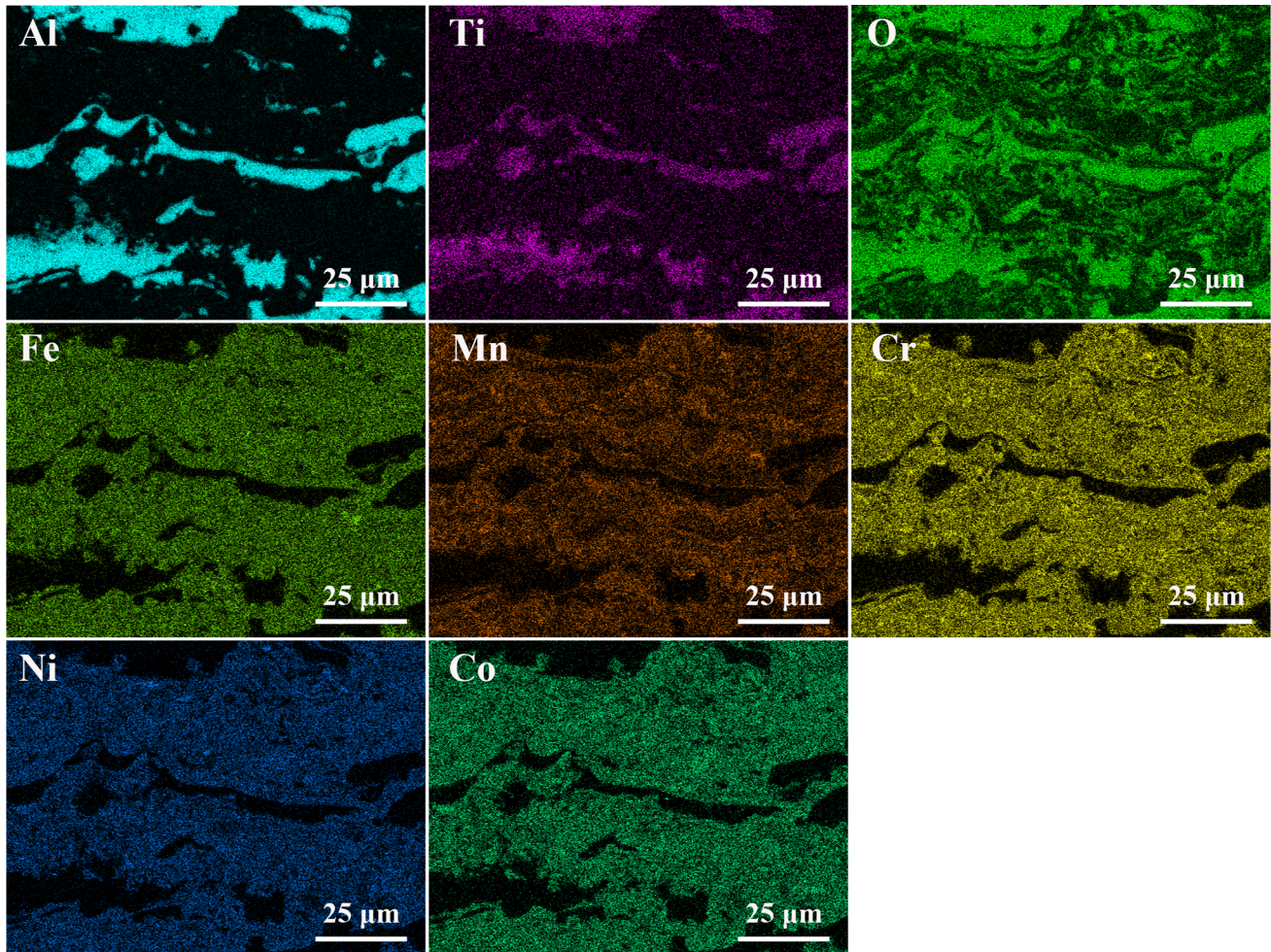


Fig. 3 Cross-sectional SEM images of the coatings: (a) and (c) pure HEA coating; (b) and (d) HEA-10 composite coating

Table 2 Chemical compositions of different regions in Fig. 3 (wt.%)

Coatings	Elements Regions	O	Al	Ti	Cr	Mn	Fe	Co	Ni
Pure HEA	A	1.63	14.36	6.32	24.32	26.61	26.76
	B	18.88	14.05	4.19	19.36	21.40	21.56
HEA-10	C	2.79	0.81	...	11.98	3.95	23.34	28.15	28.98
	D	21.65	1.26	...	18.39	4.98	18.76	17.76	17.20
	E	42.21	43.87	10.15	0.74	0.01	1.37	0.79	0.86

**Fig. 4** EDS maps of the HEA-10 composite coating corresponding to Fig. 3(d)

results indicate that the addition of Al_2O_3 -13wt.% TiO_2 powders did not change the composition of the CoCr-FeMnNi HEA matrix.

Figure 5(a) shows a high-magnification image of the HEA-10 composite coating. Figure 5(a) indicates that the microstructure of the Al_2O_3 - TiO_2 layer was three-dimensional (3D) network structure. The submicron grains (approximately 500 nm) and thin net walls (thickness less than 50 nm) combined to form the 3D network structure. Some studies have shown that the particulate structure in plasma-

sprayed coatings was formed by the partially melted Al_2O_3 -13wt.% TiO_2 powders, and the 3D network structure may enhance the toughness of the coating by increasing the resistance of crack propagation (Ref 28, 29). Furthermore, Fig. 5(a) shows that the layered HEA matrix was tightly bound by the Al_2O_3 - TiO_2 phase, and the gaps and vacancies between the layers were filled, which contributed to the obvious improvement in coating densification (Ref 30). Figure 5(b) shows the TEM micrograph of the Al_2O_3 - TiO_2 phase in the HEA-10 composite coating. The selected area

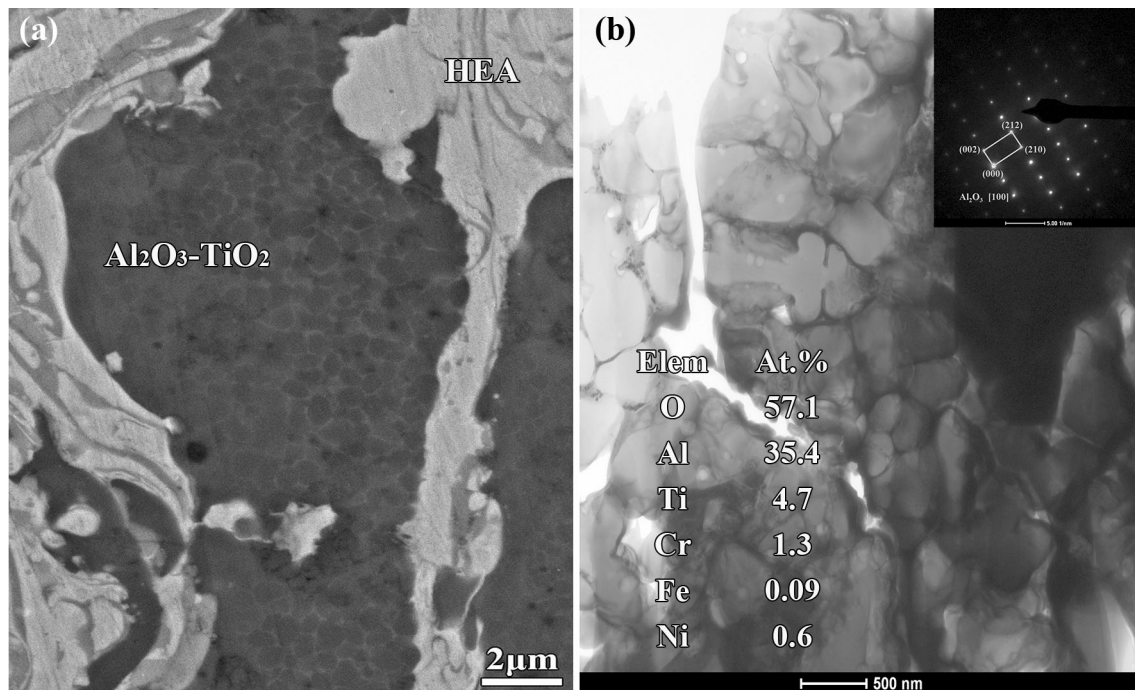


Fig. 5 (a) High magnification of the HEA-10 coating and (b) TEM micrographs of the $\text{Al}_2\text{O}_3\text{-TiO}_2$ phase in the HEA-10 coating

diffraction (SAD) patterns in Fig. 5(b) illustrated that the nanoparticles were mainly $\alpha\text{-Al}_2\text{O}_3$, which was consistent with the XRD patterns. Additionally, the EDS results (in Fig. 5b) show that some Ti was dissolved in the Al_2O_3 phase (Ref 31), which indicated that the $\text{Al}_2\text{O}_3\text{-13wt.\%TiO}_2$ powders were melted during the spraying process.

Figure 6(a) shows the indentation–load curves of the substrate, the pure HEA coating and HEA-10 coating. Compared with those of the pure HEA coating, the maximum indentation depths of the HEA-10 coating decreased from 640 nm to 591 nm. Figure 6(b) shows the hardness (H) and elastic modulus (E) of the substrate, the pure HEA coating and the HEA-10 coating. The hardness of the HEA-10 coating was 7.525 GPa, which is an improvement of 28.92% compared with the pure HEA coating due to the reinforcement of the 3D network of the $\text{Al}_2\text{O}_3\text{-TiO}_2$ phase. There was no significant difference in the elastic modulus values of the substrate and the as-sprayed coating. Thus, the interface of the substrate and coatings was well bonded. Figure 6(c) shows the H/E ratio and H^3/E^2 ratio of the as-sprayed coatings. The H/E ratio is widely used as a valuable measure in determining the limit of elastic behavior in a surface contact. A higher H/E ratio can promote the material to elastically recover the deformation induced by external stress (Ref 32). H^3/E^2 is also related to the wear characteristics, representing the resistance to plastic deformation in the loaded contact (Ref 33). Thus, the HEA-10 composite coating with high H/E and H^3/E^2 values may

present high wear resistance during sliding wear contacts. Figure 6(d) shows the η of the as-sprayed coatings, where η is the ratio of the elastic work (E_{elasti} , area of S_1 in Fig. 6a) and total work (E_{total} , area of $S_1 + S_2$ in Fig. 6a) performed during the indentation, representing a measure of the surface elastic property of a material (Ref 34). Accordingly, η can be used to analyze the elastic effects of the composite coating on the wear resistance. Cheng et al. (Ref 13) reported that the wear resistance of the coatings is proportional to the H/E ratio and η value. Figure 6(d) indicates that the η value of the HEA-10 coating was 1.26 times that of the pure HEA coating, meaning that the elastic recovery of the HEA-10 composite coating was better than that of the pure HEA coating. Figure 7 shows the microhardness measured across the cross sections of the as-sprayed coatings and the substrate. The results indicated that the $\text{Al}_2\text{O}_3\text{-TiO}_2$ phase significantly enhanced the hardness of the CoCrFeMnNi HEA coating. Therefore, the nanoindentation results and the microhardness of the as-sprayed coatings demonstrated that the $\text{Al}_2\text{O}_3\text{-TiO}_2$ phase had a positive effect in decreasing the friction coefficient and enhancing wear resistance of the composite coating.

Friction and Wear Behaviors of the Coatings

Figure 8 shows the friction coefficient variation in the as-sprayed coatings under different sliding temperatures. All the friction coefficient curves can be divided into running-in and steady-state periods (Ref 35). The friction

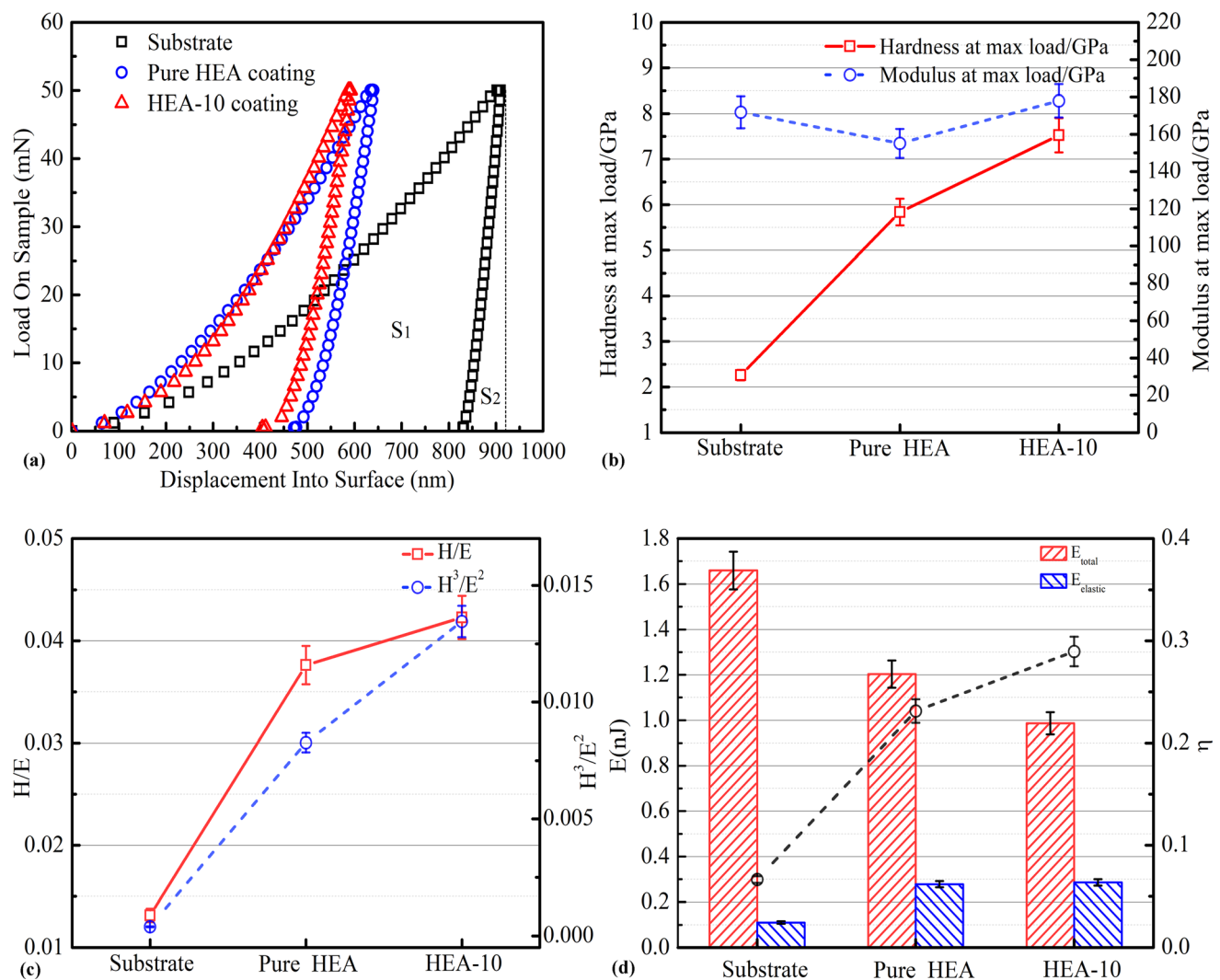


Fig. 6 Nanoindentation test results of the coatings: (a) the load–displacement curves; (b) H and E; (c) H/E and H^3/E^2 ; and (d) the mean elastic performance of indentation

coefficients of the as-sprayed coatings were in the range of 0.20–0.30. The friction coefficients of both the pure HEA coatings and HEA-10 coatings showed a trend of first decreasing and then increasing with increasing sliding temperature. The decrease in the friction coefficient was mainly due to the oxide film that was formed on the surface (Ref 25). However, the hardness of the as-sprayed coatings decreased with sliding temperature, which led to high adhesion between the wear surfaces and Si_3N_4 sphere. Thus, the friction coefficient increased with the sliding temperature. Additionally, the high hardness of the HEA-10 coatings caused by the Al_2O_3 - TiO_2 phase (Fig. 7) can reduce adhesion during friction. Thus, the friction coefficients of the HEA-10 coatings were lower than those of the pure HEA coatings under the same sliding conditions. Furthermore, the fluctuation in the friction coefficient curve of the HEA-10 coating was smaller than that in the pure

HEA coating during the steady wear stage at 600 °C. Figure 9 presents the 3D surface topographies of the worn scars of the pure HEA and HEA-10 coatings under sliding motions at different temperatures. The width and depth of the wear scars of pure HEA coatings decreased with the wear temperature. However, the width and depth of the wear scars for HEA-10 coatings were stable at elevated sliding temperatures. Moreover, the width and depth of the wear scars of the HEA-10 coatings were smaller than those of the pure HEA coating. Figure 10 shows the wear rates of the as-sprayed coatings under sliding motions at different temperatures. The pure HEA coating exhibits a significant reduction in wear rate with increasing temperature. The wear rates of the HEA-10 composite coating under elevated temperature were appreciably lower than those of the pure HEA coating, which corresponded to the above nanoindentation and microhardness test results (Fig. 6 and

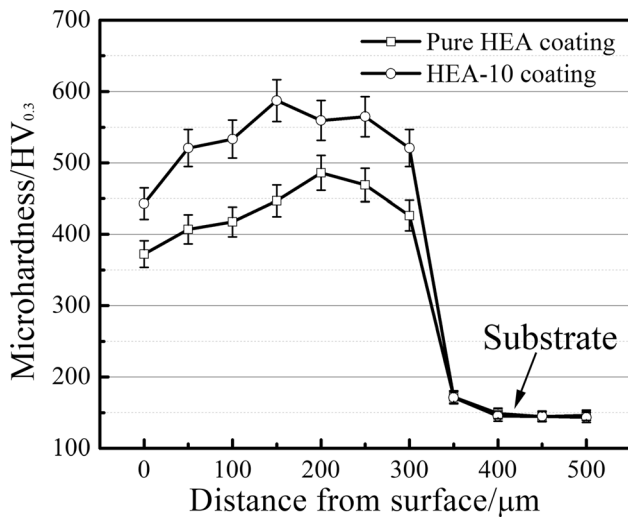


Fig. 7 Microhardness distributions along the depth direction in the cross section of the as-sprayed coatings

7). Additionally, the wear rates of HEA-10 decreased first and then increased with increasing temperature. The lowest wear rate of the HEA-10 coating was $9.86 \times 10^{-6} \text{ mm}^3 \cdot \text{N}^{-1} \cdot \text{m}^{-1}$ at 200 °C. The lower friction coefficient of the HEA-10 coating at 200 °C (Fig. 8b) indicated that the oxide film on the friction surface was stable. In addition, the higher hardness of the HEA-10 coating than the pure HEA coating reduced the adhesion and spallation of the oxide film during sliding at 200 °C. The stable oxide film had a good protective effect on the coating. However, for ceramics, the reduction effect on adhesion decreased with increasing sliding temperature. Thus, the spalling of the oxide film was increased, and the wear resistance of the coating was decreased.

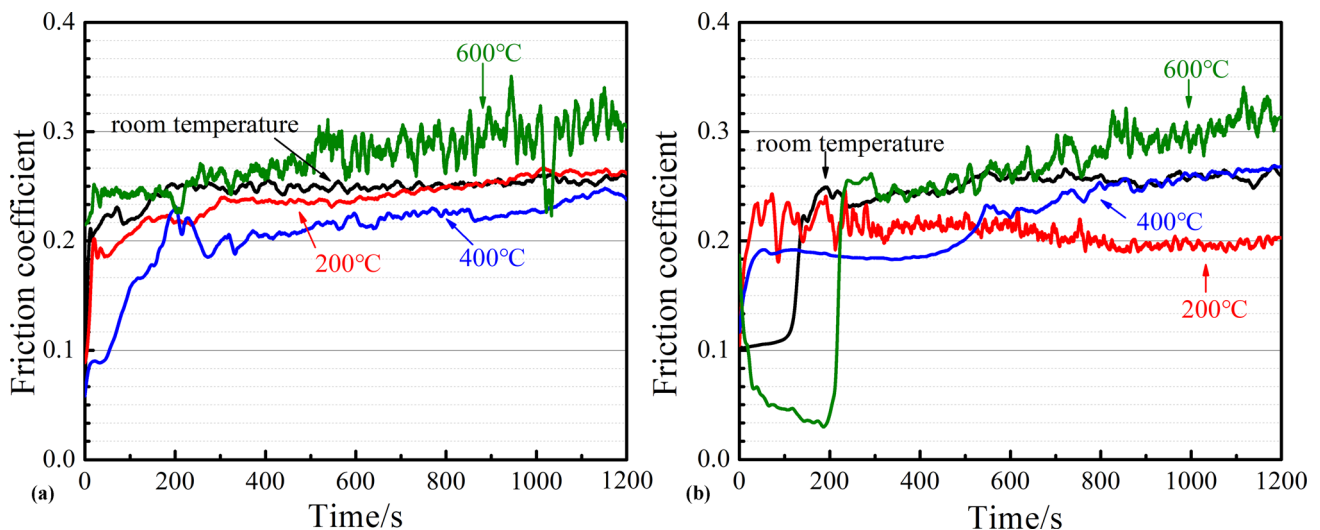


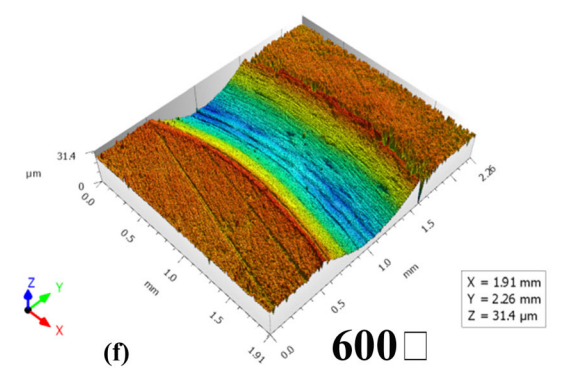
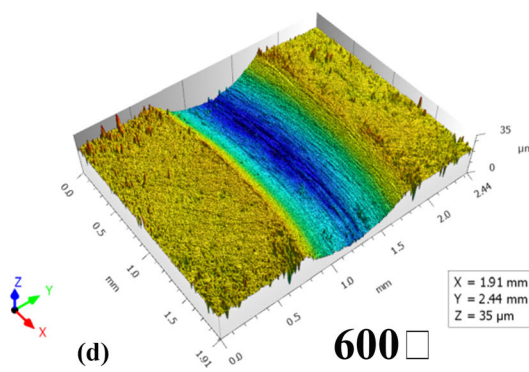
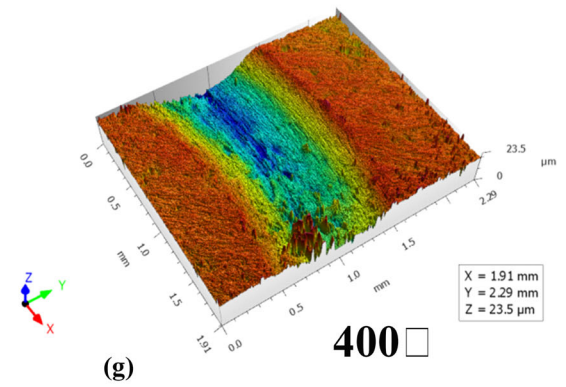
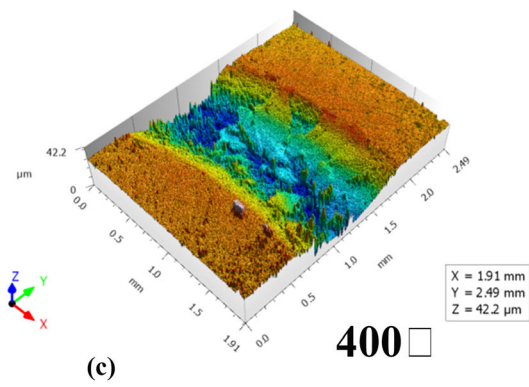
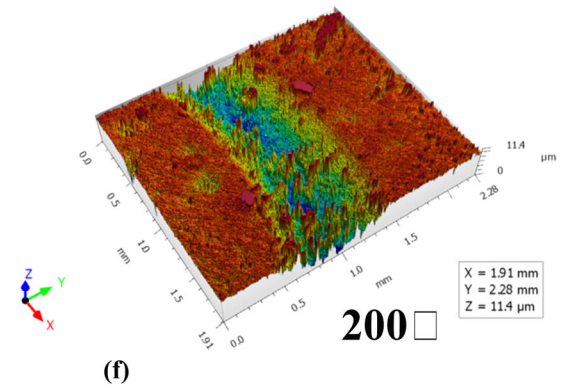
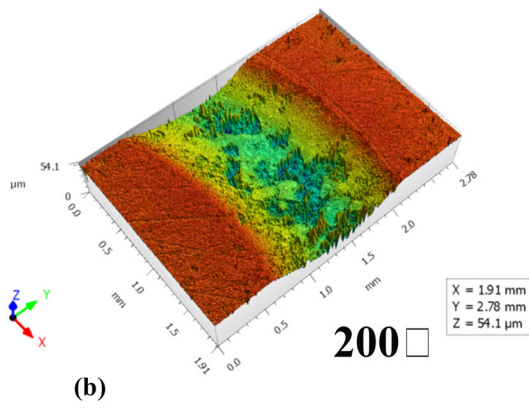
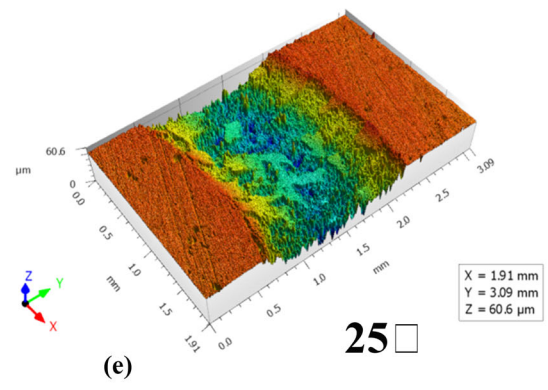
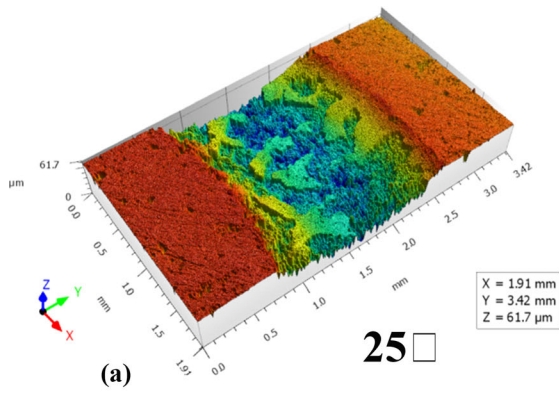
Fig. 8 Friction coefficient (COF) curves of coatings sliding under various conditions: (a) pure HEA coating and (b) HEA-10 composite coating

Fig. 9 3D surface topographies of worn surfaces sliding under different temperatures, (a)-(d) the pure HEA coatings and (e)-(h) the HEA-10 coatings

Worn Surface Morphology and Wear Mechanism

Figures 11 and 12 shows the worn surfaces of the pure HEA coating and HEA-10 composite coating, respectively. The low-magnification images of worn surfaces (the inset in Figs. 11 and 12) show that the worn surfaces of the two HEA coatings contained adhesive layers (Ref 36). The small amount of Si on the worn surfaces (the EDS results shown in Tables 3 and 4) illustrated that there was some material transfer between the friction samples and the opposite grinding part during the wear process. Thus, the adhesive wear process occurred during sliding at different temperatures. Figures 11(a)-(c) and 12(a)-(c) displays some oxidation sheets, craters and a few cracks on the worn surface. Figures 11(d) and 12(d) presents some grooves, small oxidation sheets and some debris that were present on the worn surfaces subjected to sliding at 600 °C. Therefore, the wear mechanisms of the as-sprayed coatings can be regarded as adhesive wear, oxidation wear and abrasive wear (Ref 37, 38). Furthermore, Fig. 12 reveals smoother worn surfaces of the HEA-10 coating than of the pure HEA coating, and this effect was caused by the reinforcement of the Al₂O₃-TiO₂ phase.

Figure 13(a)-(d) and (e)-(h) shows SEM photographs of cross-sectional wear tracks of the pure HEA coatings and HEA-10 coatings subjected to sliding at different temperatures. The oxide films on the worn surfaces were obvious, and the oxide film thickness of the HEA-10 coatings was smaller than that of the pure HEA coatings. Moreover, the



oxide films on the worn surfaces of the two coatings showed loose sliding characteristics at 25–400°C, and the oxide films were dense at 600 °C. Figure 13(d) and

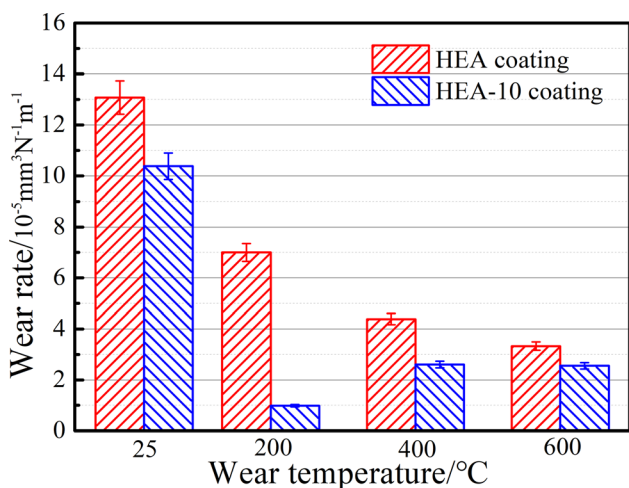


Fig. 10 Wear rate of the coatings under sliding at different temperatures

(h) shows that a plastically deformed zone appeared under the worn surface when sliding at 600 °C. The local magnification image of the cross-sectional wear tracks for the HEA coating and HEA-10 composite coating sliding at 600 °C was characterized to further clarify the wear mechanism, which is presented in Fig. 14. The EDS results of the oxide layers on the worn surfaces and the unaffected areas in the coating are shown in Fig. 14(a) and (c). The comparison of the elemental compositions of the different regions in the two coatings indicated that the wear surfaces were covered with a dense oxide film and some Al_2O_3 phases were contained in the oxide layers of the HEA-10 coating. The Al_2O_3 phase may enhance the protective functions of the oxide layers (Ref 19). Moreover, Fig. 14(b) and (d) indicates that the grains in the coatings were refined in plastic deformation zone due to dynamic recrystallization during sliding at 600 °C (Ref 37), which was beneficial for improving the resistance to plastic deformation.

In the composite coatings, the $\text{Al}_2\text{O}_3\text{-TiO}_2$ ceramic phase played a load-bearing role and served as a lubricant,

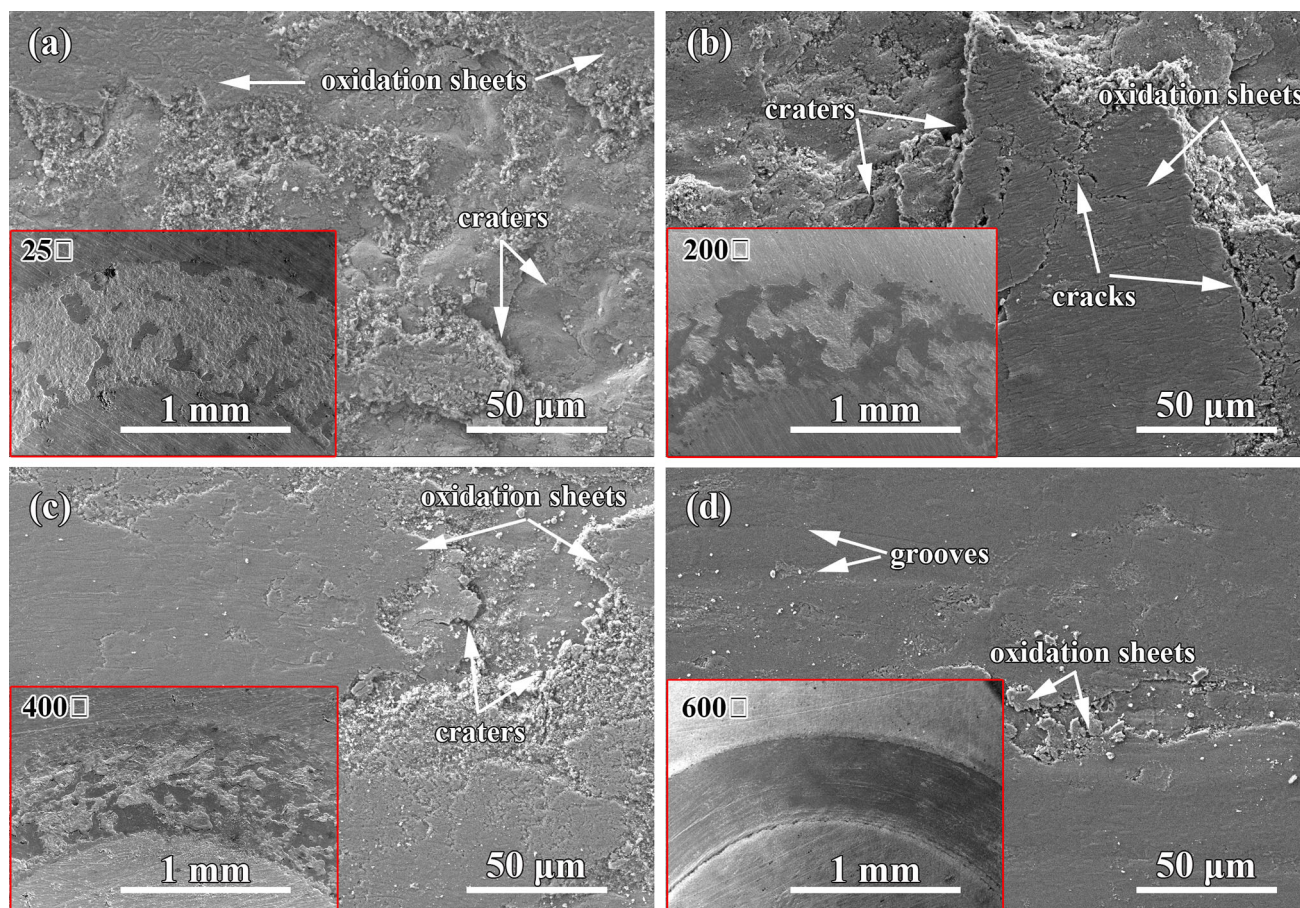


Fig. 11 Worn morphology of pure HEA coatings under sliding at different temperatures

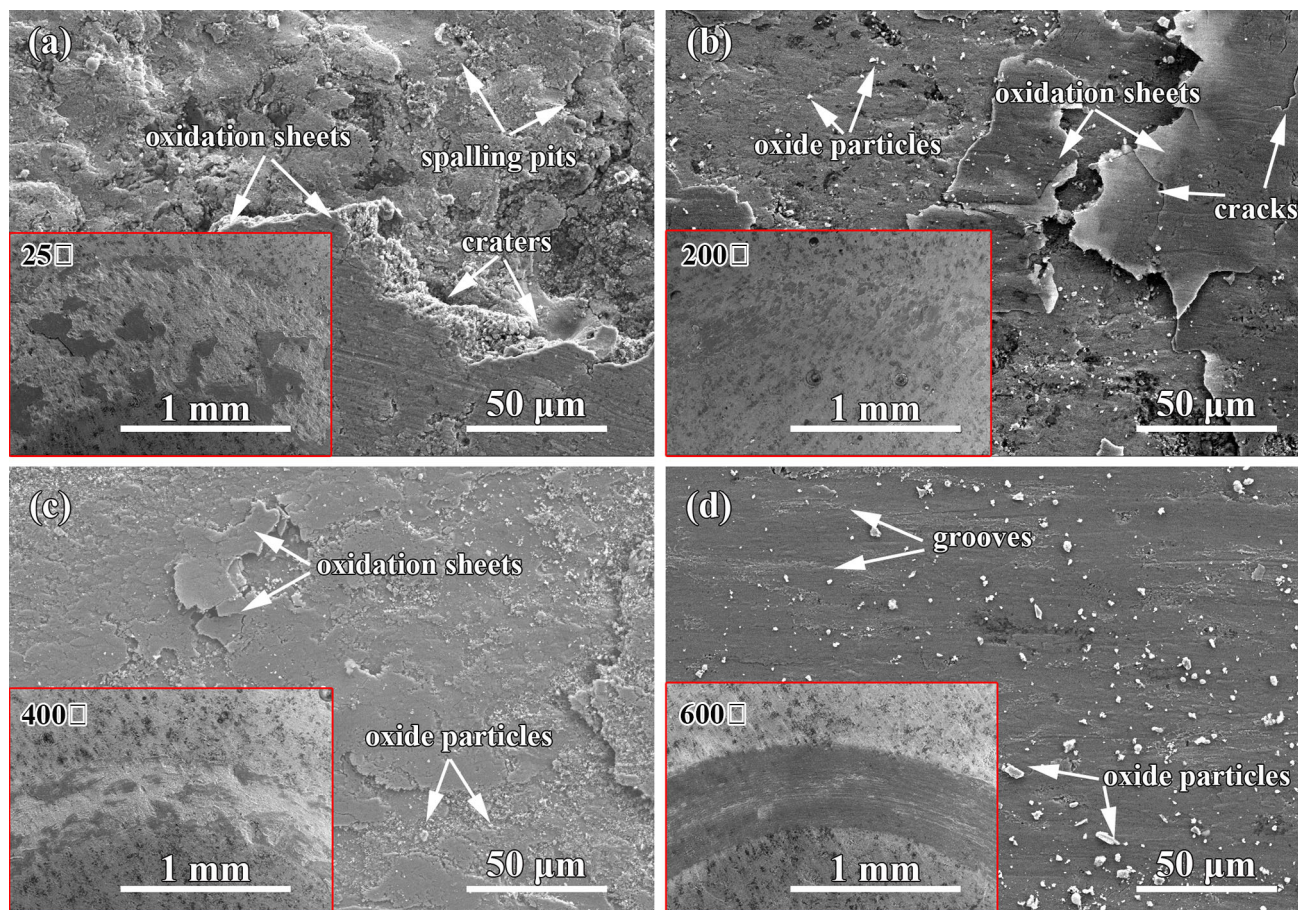


Fig. 12 Worn morphology of HEA-10 coatings under sliding at different temperatures

Table 3 Chemical composition of various worn regions for the pure HEA coating (wt.%)

Elements Temperature	C	O	Si	Cr	Mn	Fe	Co	Ni
25 °C	5.63	25.66	0.93	13.88	4.32	16.16	16.53	16.27
200 °C	6.28	24.01	0.81	13.54	4.82	16.37	16.66	17.00
400 °C	4.56	22.84	0.76	14.59	4.85	16.60	17.44	17.84
600 °C	3.04	25.20	...	12.68	5.05	17.60	18.72	17.21

Table 4 Chemical composition of various worn regions for the HEA-10 coatings (wt.%)

Elements Temperature	C	O	Al	Si	Ti	Cr	Mn	Fe	Co	Ni
25 °C	5.23	25.26	5.38	0.84	0.84	13.08	4.91	14.99	14.42	15.04
200 °C	7.63	22.13	7.60	0.52	1.10	11.70	3.13	14.47	15.40	16.31
400 °C	3.37	25.62	4.45	1.48	0.81	12.80	4.56	15.46	15.59	15.86
600 °C	2.86	25.79	3.27	0.24	...	13.56	4.68	16.60	16.28	16.72

and it reduced the real contact area and adhesion (Ref 23, 39). The results of the wear rates (Fig. 10) and the morphologies of the cross-sectional wear tracks of the as-sprayed coatings (Fig. 13 and 14) illustrated that the $\text{Al}_2\text{O}_3\text{-TiO}_2$ phase in the composite coating contributed to the low and stable friction coefficient and enhanced the

wear resistance at low temperatures. However, the excellent wear resistance of the as-sprayed coating at high temperatures was mainly due to the formation of oxide layer on the worn surface.

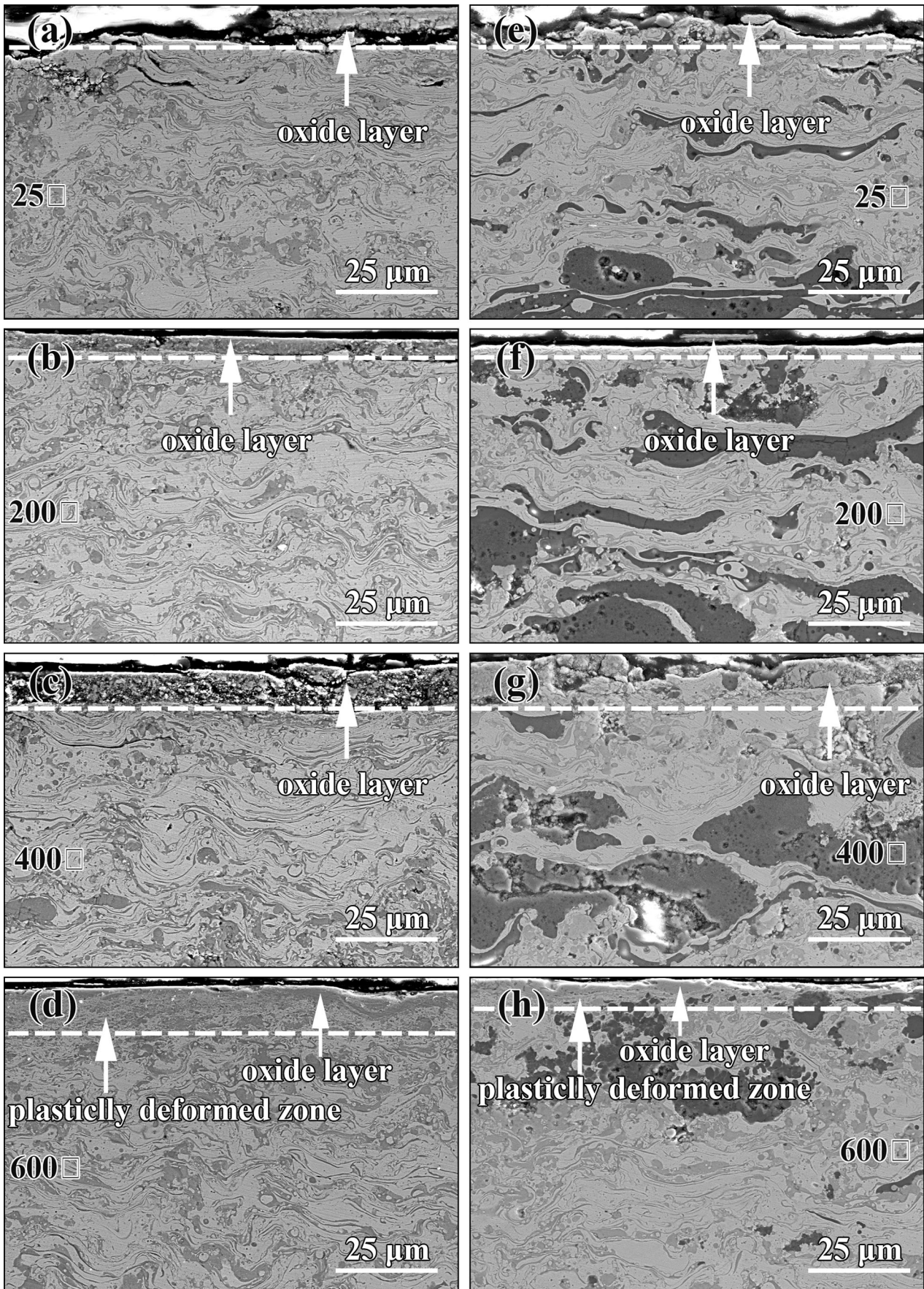


Fig. 13 Cross-sectional morphology of the worn subsurface that was sliding under different temperatures, (a)–(d) the pure HEA coatings and (e)–(h) the HEA-10 coatings

Conclusions

In this study, CoCrFeMnNi/(Al₂O₃-TiO₂) composite coatings were prepared by plasma spraying. The tribological behavior of the coatings was analyzed by sliding wear testing in the temperature range of 25–600 °C. The main findings of the study are as follows:

1. The CoCrFeMnNi/(Al₂O₃-TiO₂) composite coatings consisted of HEA layers with a single-phase FCC structure and an Al₂O₃-TiO₂ phase with a 3D network structure. The Al₂O₃-13wt.%TiO₂ ceramic powders did not significantly affect the composition and structure of the HEA matrix. The hardness of the composite coating was enhanced 1.29 times compared with that of the pure HEA coating due to the reinforcement by the Al₂O₃-TiO₂ phase. Nanoindentation experiments revealed that the Al₂O₃-TiO₂ phase

improved the plastic deformation resistance and reduced the elastic recovery resistance of the composite coatings.

2. The wear mechanisms of the CoCrFeMnNi/(Al₂O₃-TiO₂) composite coatings were adhesive and have oxidation and abrasive wear. The 3D network of the Al₂O₃-TiO₂ phase reduced the adhesion wear. The wear rates of the composite coating were lower than those of the pure HEA coating under the same sliding conditions. The Al₂O₃-TiO₂ phase contributed to the low and stable friction coefficient of the composite coatings and enhanced the wear resistance at low temperatures. The formation of an oxide layer on the worn surface contributed to the excellent wear resistance of the as-sprayed coating at high temperatures.

Acknowledgments This research work is supported by the National Key R&D Program of China (2018YFC1902404), National Natural Science Foundation of China (51775259), Natural Science Foundation of Jiangsu Province (BE2018091) and the Six Talent Peaks Project in Jiangsu Province.

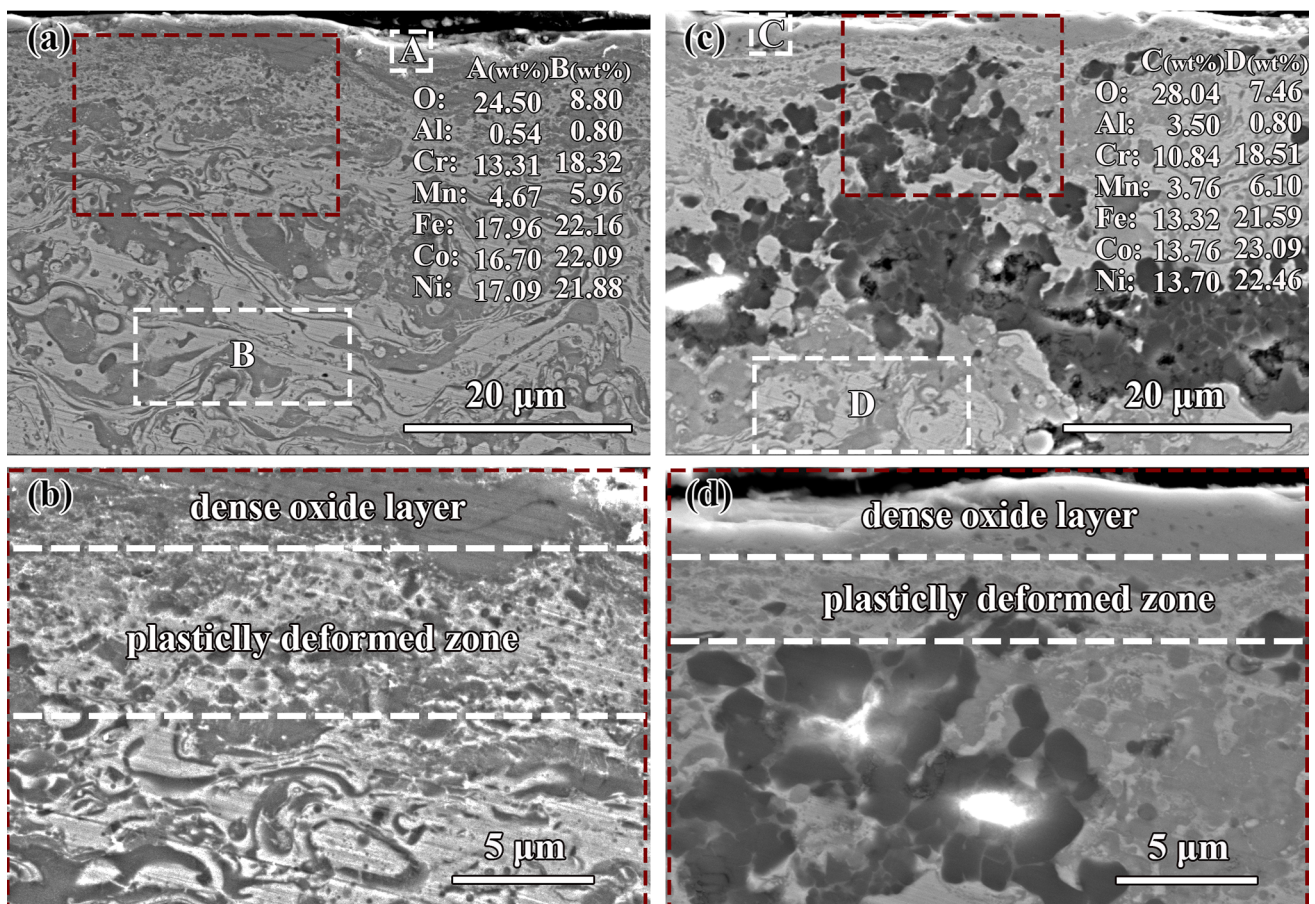


Fig. 14 Local magnification cross-sectional wear tracks of the pure HEA coating and HEA-10 composite coating at 600 °C: (a, b) pure HEA coating and (c, d) HEA-10 coating

References

- J.W. Yeh, S.K. Chen, S.J. Lin, J.Y. Gan, T.S. Chin, T.T. Shun, C.H. Tsau, and S.Y. Chang, Nanostructured High-entropy Alloys with Multiple Principal Elements: Novel Alloy Design Concepts and Outcomes, *Adv. Eng. Mater.*, 2004, **6**(5), p 299-303
- B. Cantor, I.T.H. Chang, P. Knight, and A.J.B. Vincent, Microstructural Development in Equiatomic Multicomponent Alloys, *Mater. Sci. Eng. A*, 2004, **375**, p 213-218
- Z. Lyu, C. Lee, S. Wang, X. Fan, J.W. Yeh, and P.K. Liaw, Effects of Constituent Elements and Fabrication Methods on Mechanical Behavior of High-Entropy Alloys: A Review, *Metall. Mater. Trans. A*, 2019, **50**(1), p 1-28
- A. Meghwal, A. Anupam, B.S. Murty, C.C. Berndt, R.S. Kottada, and A.S.M. Ang, Thermal Spray High-Entropy Alloy Coatings: A Review, *J. Therm. Spray Tech.*, 2020, **29**, p 857-893
- D.B. Miracle and O.N. Senkov, A Critical Review of High Entropy Alloys and Related Concepts, *Acta Mater.*, 2017, **122**, p 448-511
- J. Li, Y. Huang, X. Meng, and Y. Xie, A Review on High Entropy Alloys Coatings: Fabrication Processes and Property Assessment, *Adv. Eng. Mater.*, 2019, **21**(8), p 1900343
- J. Cheng, Y. Feng, C. Yan, X. Hu, R. Li, and X. Liang, Development and Characterization of Al-Based Amorphous Coating, *JOM*, 2019, **72**(2), p 745-753
- Z. Piao, B. Xu, H. Wang, and X. Yu, Rolling Contact Fatigue Behavior of Thermal-Sprayed Coating: A Review, *Crit. Rev. Solid State*, 2019, **2019**, p 1-28
- Y. Han, H. Chen, D. Gao, G. Yang, B. Liu, Y. Chu, J. Fan, and Y. Gao, Microstructural Evolution of NiCoCrAlHfYSi and NiCoCrAlTaY Coatings Deposited by AC-HVAF and APS, *J. Therm. Spray Techn.*, 2017, **26**(8), p 1-18
- J. Xiao, H. Tan, Y. Wu, J. Chen, and C. Zhang, Microstructure and Wear Behavior of FeCoNiCrMn High Entropy Alloy Coating Deposited by Plasma Spraying, *Surf. Coat. Tech.*, 2020, **385**, p 125430
- A.S.M. Ang, C.C. Berndt, M.L. Sesso, A. Anupam, S. Praveen, and R.S. Kottada, Plasma-Sprayed High Entropy Alloys: Microstructure and Properties of AlCoCrFeNi and MnCoCrFeNi, *Metall. Mater. Trans. A*, 2015, **46**(2), p 791-800
- C. Wang, J. Yu, Y. Zhang, and Y. Yu, Phase Evolution and Solidification Cracking Sensibility in Laser Remelting Treatment of the Plasma-Sprayed CrMnFeCoNi High Entropy Alloy Coating, *Mater. Des.*, 2019, **182**, p 108040
- A. Piglionne, B. Dovggy, C. Liu, C.M. Gourlay, P.A. Hooper, and M.S. Pham, Printability and Microstructure of the CoCrFeMnNi High-Entropy Alloy Fabricated by Laser Powder Bed Fusion, *Mater. Lett.*, 2018, **224**, p 22-25
- J. Ahn, Y.K. Kim, S.H. Yoon, and K.A. Lee, Tuning the Microstructure and Mechanical Properties of Cold Sprayed Equiatomic CoCrFeMnNi High-Entropy Alloy Coating Layer, *Met. Mater. Int.*, 2020, **2020**, p 1-10
- J. Cheng, D. Liu, X. Liang, and Y. Chen, Evolution of Microstructure and Mechanical Properties of In Situ Synthesized TiC-TiB₂/CoCrCuFeNi High Entropy Alloy Coatings, *Surf. Coat. Tech.*, 2015, **281**, p 109-116
- J. Wang, B. Zhang, Y. Yu, Z. Zhang, S. Zhu, X. Lou, and Z. Wang, Study of High Temperature Friction and Wear Performance of (CoCrFeMnNi)₈₅Ti₁₅ High-entropy Alloy Coating Prepared by Plasma Cladding, *Surf. Coat. Tech.*, 2020, **384**, p 125337
- L. Jiang, W. Wu, Z. Cao, D. Deng, and T. Li, Microstructure Evolution and Wear Behavior of the Laser Cladded CoFeNi₂V_{0.5}Nb_{0.75} and CoFeNi₂V_{0.5}Nb High-entropy Alloy Coatings, *J. Therm. Spray Tech.*, 2016, **25**(4), p 806-814
- H. Liu, J. Liu, P. Chen, and H. Yang, Microstructure and High Temperature Wear Behaviour of In-situ TiC Reinforced AlCoCrFeNi-based High-entropy Alloy Composite Coatings Fabricated by Laser Cladding, *Opt. Laser Technol.*, 2019, **118**, p 140-150
- S. Wang, Q. Zhao, D. Liu, and N. Du, Microstructure and Elevated Temperature Tribological Behavior of TiO₂/Al₂O₃ Composite Ceramic Coating Formed by Microarc Oxidation of Ti6Al4V Alloy, *Surf. Coat. Tech.*, 2015, **272**, p 343-349
- W. Tian, Y. Wang, and Y. Yang, Three Body Abrasive Wear Characteristics of Plasma Sprayed Conventional and Nanostructured Al₂O₃-13%TiO₂ Coatings, *Tribol. Int.*, 2010, **43**(5), p 876-881
- V.F. Gorban, N.A. Krapivka, M.V. Karpets, A.D. Kostenko, A.N. Samelyuk, and E.V. Kantsyr, Effect of Temperature on Wear Behavior of High-entropy Alloys, *J. Frict. Wear*, 2017, **38**(4), p 292-296
- G. Deng, A.K. Tieu, X. Lan, L. Su, L. Wang, Q. Zhu, and H. Zhu, Effects of Normal Load and Velocity on the Dry Sliding Tribological Behaviour of CoCrFeNiMo_{0.2} High Entropy Alloy, *Tribol. Int.*, 2020, **144**, p 106116
- G. Jin, Z. Cai, Y. Guan, X. Cui, Z. Liu, Y. Li, M. Dong, and D. Zhang, High Temperature Wear Performance of Laser-cladded FeNiCoAlCu High-entropy Alloy Coating, *Appl. Surf. Sci.*, 2018, **445**, p 113-122
- S. Yang, Z. Liu, and J. Pi, Microstructure and Wear Behavior of the AlCrFeCoNi High-Entropy Alloy Fabricated by Additive Manufacturing, *Mater. Lett.*, 2019, **261**, p 127004
- J. Joseph, N. Haghdadi, K. Shamlaye, P. Hodgson, M. Barnett, and D. Fabijanic, The Sliding Wear Behaviour of CoCrFeMnNi and Al_xCoCrFeNi High Entropy Alloys at Elevated Temperatures, *Wear*, 2019, **428**, p 32-44
- Z. Chu, X. Zheng, C. Zhang, J. Xu, and L. Gao, Study the Effect of AT13 Addition on the Properties of AT13/Fe-based Amorphous Composite Coatings, *Surf. Coat. Tech.*, 2019, **379**, p 125053
- A. Anupam, R.S. Kottada, S. Kashyap, A. Meghwal, B.S. Murty, C.C. Berndt, and A.S.M. Ang, Understanding the Microstructural Evolution of High Entropy Alloy Coatings Manufactured by Atmospheric Plasma Spray Processing, *Appl. Surf. Sci.*, 2019, **505**, p 144117
- Y. Yang, Y. Wang, W. Tian, D. Yan, J. Zhang, and L. Wang, Influence of Composite Powders' Microstructure on the Microstructure and Properties of Al₂O₃-TiO₂ Coatings Fabricated by Plasma Spraying, *Mater. Design*, 2015, **65**, p 814-822
- Y. Wang, W. Tian, and Y. Yang, Thermal Shock Behavior of Nanostructured and Conventional Al₂O₃/13 wt% TiO₂ Coatings Fabricated by Plasma Spraying, *Surf. Coat. Tech.*, 2007, **201**(18), p 7746-7754
- H. Luo, P. Song, A. Khan, J. Feng, J.J. Zang, X.P. Xiong, J.G. Lü, and J.S. Lu, Alternant Phase Distribution and Wear Mechanical Properties of an Al₂O₃-40 wt%TiO₂ Composite coating, *Ceram. Int.*, 2017, **43**(9), p 7295-7304
- D. Goberman, Y. Sohn, L. Shaw, E. Jordan, and M. Gell, Microstructure Development of Al₂O₃-13wt.%TiO₂ Plasma Sprayed Coatings Derived from Nanocrystalline Powders, *Acta Mater.*, 2002, **50**(5), p 1141-1152
- B.D. Beake, V.M. Vishnyakov, and A.J. Harris, Relationship between Mechanical Properties of Thin Nitride-Based Films and Their Behaviour in Nano-Scratch Tests, *Tribol. Int.*, 2011, **44**(4), p 468-475
- J. Musil, F. Kunc, H. Zeman, and H. Polakova, Relationships Between Hardness, Young's Modulus and Elastic Recovery in Hard Nanocomposite Coatings, *Surf. Coat. Tech.*, 2002, **154**(2-3), p 304-313

34. R.J. Hudson, P. Zioupos, and P.P. Gill, Investigating the Mechanical Properties of RDX Crystals Using Nano-Indentation, *Propell. Explos. Pyrot.*, 2012, **37**(2), p 191-197
35. D.D. Liang, X.S. Wei, T.C. Ma, B. Chen, H.R. Jiang, Y. Dong, and J. Shen, Sliding Tribocorrosion Behavior of Fe-Based Bulk Metallic Glass under Corrosive Environments, *J. Non-Cryst. Solids*, 2019, **510**, p 62-70
36. Z. Xiang, X. Liu, J. Ren, J. Luo, S. Shi, Y. Chen, G. Lian, S. Shao, and H. Wu, Investigation of Laser Cladding High Temperature Anti-wear Composite Coatings on Ti6Al4V Alloy with the Addition of Self-lubricant CaF₂, *Appl. Surf. Sci.*, 2014, **313**, p 243-250
37. Y.H. Lv, J. Li, Y.F. Tao, and L.F. Hu, High-temperature Wear and Oxidation Behaviors of TiNi/Ti₂Ni Matrix Composite Coatings with TaC Addition Prepared on Ti6Al4V by Laser Cladding, *Appl. Surf. Sci.*, 2017, **402**, p 478-494
38. M. Annasamy, N. Haghdadi, A. Taylor, P. Hodgson, and D. Fabijanic, Dynamic Recrystallization Behaviour of Al_xCoCrFeNi High Entropy Alloys during High-temperature Plane Strain Compression, *Mater. Sci. Eng., A*, 2019, **745**, p 90-106
39. T. Luo, X. Wei, H. Zhao, G. Cai, and X. Zheng, Tribology Properties of Al₂O₃/TiO₂ Nanocomposites as Lubricant Additives, *Ceram. Int.*, 2014, **40**(7), p 10103-10109

Publisher's Note Springer Nature remains neutral with regard to jurisdictional claims in published maps and institutional affiliations.